

SEMI-ANALYTIC PRELIMINARY DESIGN OF LOW-THRUST MISSIONS

Javier Roa*, Anastassios E. Petropoulos[†] and Ryan S. Park[‡]

Using generalized logarithmic spirals to approximate low-thrust trajectories, a new strategy for the design of low-thrust gravity-assist transfers has been developed. Each transfer leg is defined by a semi-analytic model, and its solution is equivalent to a hybrid Lambert's problem. The method is suitable for approximating both flyby and rendezvous transfer legs. A branch and prune algorithm is used to generate a collection of initial guesses for further optimization. The analytic nature of the low-thrust model simplifies the pruning step, since dynamical and operational constraints (like maximum thrust or total Δv) can be imposed easily. The solutions obtained with the global search algorithm can be post-processed, filtered, and ranked according to various criteria. This is where the versatility of the method resides, because changing the selection criteria does not require a new search. Selected candidates are then optimized further, in order to generate actual low-thrust orbits. Two mission design examples are presented: an asteroid deflection mission using a kinetic impactor, and a rendezvous mission to Jupiter. These examples are used to analyze the convergence of the optimization stage, in particular how far from the optimal solution the initial guesses are.

INTRODUCTION

The preliminary design of low-thrust gravity-assist missions typically involves two stages: a global exploration of the space of solutions in order to generate initial guesses, and the actual optimization of candidate orbits. Various techniques are available to conduct searches and evaluate the performance of different solutions, ranging from heuristic algorithms for global optimization to direct searches controlling the dimension of the problem.^{1,2}

Because hundreds of thousands or even millions of missions will be evaluated during the exploration phase, simplified approximate models are often used to model low-thrust legs. In this context, shape-based methods stand out as interesting tools for approximating continuous-thrust transfers. The orbit is assumed to have a certain shape, and the thrust profile required to follow such orbit is computed a posteriori. Exponential sinusoids³ are a good example of a shape-based method that has been successfully applied to many design scenarios, like the reformulation of Lambert's problem in the low-thrust realm.⁴ A number of reviews of existing analytic solutions and shape-based algorithms can be found in the literature.^{5,6} Pseudo-equinoctial elements exploit the use of non-osculating elements to model low-thrust trajectories, and result in a flexible design tool.⁷ An

*Post-doctoral Fellow, Solar System Dynamics Group. Jet Propulsion Laboratory, California Institute of Technology, Pasadena, CA 91109, USA. Member AIAA, javier.roa@jpl.nasa.gov.

[†]Member of Engineering Staff, Outer Planets Mission Analysis Group. Jet Propulsion Laboratory, California Institute of Technology, Pasadena, CA 91109, USA.

[‡]Group Supervisor, Solar System Dynamics Group. Jet Propulsion Laboratory, California Institute of Technology, Pasadena, CA 91109, USA.

© 2017. California Institute of Technology. Government sponsorship acknowledged.

interesting alternative is the design in the space of velocities: the orbit is modeled by shaping the velocity, instead of the actual trajectory.⁸ This hodographic method allows to find low Δv transfers easily. The Q -law algorithm⁹ focuses on targeting the orbital elements of the arrival body by minimizing the so called proximity quotient, Q , which scales with the separation from the target orbit. This algorithm provides solutions that are very close to optimal.

This paper uses a new analytic solution to a particular continuous-thrust problem, the family of generalized logarithmic spirals,¹⁰ and implements a branch and prune global search algorithm for generating initial guesses. These initial guesses will then be optimized in a second stage in order to generate potentially feasible orbits. This analytic solution is briefly introduced in the following section, and the next section explains the design strategy in detail: how each individual leg is solved, the rationale behind the branch and prune algorithm, and the selection and optimization of promising candidates. Two examples are presented in order to investigate how well does the approximate model represent the optimal solution.

Analytic Low-Thrust Model

Generalized logarithmic spirals are the parametric solutions to the dynamics perturbed by the acceleration

$$\mathbf{a}_p = \frac{\mu}{r^2}[\xi \cos \psi \mathbf{t} + (1 - 2\xi) \sin \psi \mathbf{n}], \quad (1)$$

where μ is the gravitational parameter of the central body, ψ is the flight-direction angle, and \mathbf{t} and \mathbf{n} are unit vectors directed along the tangential and normal directions. That is,

$$\mathbf{t} = \frac{\mathbf{v}}{v}, \quad \mathbf{n} = \mathbf{k} \times \mathbf{t}, \quad \mathbf{k} = \frac{\mathbf{h}}{h}, \quad \text{and} \quad \cos \psi = \frac{(\mathbf{r} \cdot \mathbf{v})}{rv},$$

with $\mathbf{h} = \mathbf{r} \times \mathbf{v}$ denoting the angular momentum vector. Figure 1 depicts the geometry of the problem referred to an inertial frame \mathfrak{S} , and θ is the polar angle. The thrust vector lies in the orbital plane, so the resulting motion is planar.

The control parameter ξ can be adjusted as required, and it affects both the magnitude and direction of the thrust vector. The complete analytic solution including the spiral Kepler equation can be found in the Appendix.

The main property of this new family of orbits is the fact that they admit two integrals of motion, which are extensions of the laws of conservation of energy and angular momentum. In particular,

$$v^2 - \frac{2\mu}{r}(1 - \xi) = K_1 \quad (2)$$

and

$$rv^2 \sin \psi = K_2 \quad (3)$$

are two first integrals written in terms of the constants of motion K_1 and K_2 . The former is the generalized energy, and the latter is the generalized angular momentum. They can be obtained from the initial conditions:

$$K_1 = v_0^2 - \frac{2\mu}{r_0}(1 - \xi)$$

$$K_2 = r_0 v_0^2 \sin \psi_0.$$

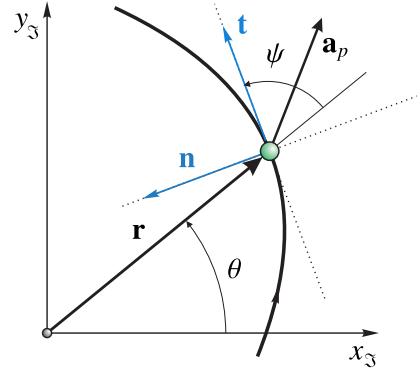


Figure 1: Geometrical definition of the problem

The analytic solution to the motion is simplified if the dynamics are formulated using a set of coordinates intrinsic to the trajectory, (r, v, θ, ψ) , instead of polar or Cartesian.

Similarity transformation

Interestingly, there is a similarity transformation that converts the problem defined by the acceleration in Eq. (1) into a simpler problem,¹¹

$$\mathcal{S} : (t; r, v, \theta, \psi) \mapsto (\tau; \tilde{r}, \tilde{v}, \theta, \psi).$$

The transformation \mathcal{S} defines the homothety

$$\tau = \frac{t}{\beta}, \quad \tilde{r} = \frac{r}{\alpha}, \quad \tilde{v} = \frac{v}{\delta},$$

in terms of the constants

$$\beta = \sqrt{\frac{\alpha^3}{2\mu(1-\xi)}}, \quad \text{and} \quad \delta = \frac{\alpha}{\beta} = \sqrt{\frac{2\mu(1-\xi)}{\alpha}}.$$

Here, α is a scaling factor (with units of longitude) that can be defined arbitrarily.

Under this transformation the solution to the problem perturbed by the parametric acceleration in Eq. (1) reduces to the normalized Kepler problem perturbed by $\tilde{\mathbf{a}}_p$,

$$\frac{d^2\tilde{\mathbf{r}}}{d\tau^2} = -\frac{\tilde{\mathbf{r}}}{\tilde{r}^3} + \tilde{\mathbf{a}}_p, \quad \text{with} \quad \tilde{\mathbf{a}}_p = \frac{\cos\psi}{2\tilde{r}^2} \mathbf{t}. \quad (4)$$

The transformed acceleration has no components along the normal direction, and it does not depend explicitly on the control parameter ξ . Once the solution to the simpler problem in Eq. (4) is known, the solution to the original problem perturbed by (1) is recovered thanks to

$$t(\theta) = \beta\tau(\theta), \quad r(\theta) = \alpha\tilde{r}(\theta), \quad v(\theta) = \delta\tilde{v}(\theta).$$

DESIGN STRATEGY

The proposed methodology for the preliminary design of low-thrust gravity-assist trajectories decomposes in two steps:

1. Global search for candidate initial guesses using generalized logarithmic spirals.
2. Local optimization of selected candidates.

The first step divides the problem in individual legs, which are modeled by combining generalized logarithmic spirals with coast arcs to approximate low-thrust legs. From a practical point of view, the user should treat the spirals just like conic sections, exploiting the extended conservation laws in Eqs. (2) and (3). The conserved quantities can be used to “patch” spiral segments with Keplerian arcs without impulsive maneuvers in the transition points.

Solving each transfer leg reduces to solving a hybrid Lambert problem, combining spiral segments with coast arcs. The solution is found with an iterative algorithm. The simplicity and robustness of the method make it a useful tool for conducting extensive searches when there is little or

no information about the optimal solution. A branch and prune algorithm has been implemented to explore different configurations of the problem, and to select promising solutions.

The search algorithm will generate a collection of candidate solutions that are post-processed and filtered in order to choose interesting candidates. These selected trajectories will be used as initial guesses for an actual optimizer. In this case, the global search tool has been integrated with JPL's preliminary design software MALTO, which implements the Sims and Flanagan algorithm.^{12,13}

Semi-Analytic Design of Individual Legs

When no control is available (Keplerian orbits), the in-plane dynamics of the spacecraft are completely determined by four constants of integration. They are typically the initial conditions $(x_0, y_0, \dot{x}_0, \dot{y}_0)$, or $(r_0, v_0, \theta_0, \psi_0)$ in intrinsic coordinates. Once the departure date is fixed, the initial position of the spacecraft (r_0, θ_0) is known from the ephemeris model. Two degrees of freedom remain, (v_0, ψ_0) . Consequently, the system admits only two additional constraints, i.e. it can only satisfy two boundary conditions. In a design problem, these two constraints force the position vector of the spacecraft to match that of the target body at the final time, $r(t_f) = r_f$ and $\theta(t_f) = \theta_f$. Since a time-explicit analytic solution to Kepler's problem is not available, it is often useful to pose the problem using the polar angle θ as independent variable:

$$\begin{aligned} r(\theta_f; v_0, \psi_0) - r_f &= 0 \\ t(\theta_f; v_0, \psi_0) - t_f &= 0. \end{aligned}$$

The relative configuration of the planets provides the boundary conditions $(r_0, \theta_0, r_f, \theta_f, t_f)$, and this system of equations can be solved for v_0 and ψ_0 ; this is none other than Lambert's problem. Because the initial velocity vector defined by (v_0, ψ_0) will not necessarily coincide with the velocity of the departure body, an impulsive maneuver that adjusts the velocity will be required. Single-impulse transfers are the simplest solution to transfer problems.

Instead of using single-impulse transfers and in order to model low-thrust trajectories, we assume that the spacecraft first traverses a generalized logarithmic spiral from θ_0 to an intermediate point θ_A , and then describes a Keplerian orbit from θ_A to θ_f , or vice-versa (see Fig. 2). This technique introduces two additional degrees of freedom in the problem: the control parameter in the spiral arc ξ , and the position of the intermediate point θ_A . Thanks to these two new degrees of freedom the velocity vector at departure (v_0, ψ_0) can be fixed, instead of being computed from the boundary-value problem. In the first leg, the user will be able to specify the launch v -infinity vector. In the following legs, the flyby geometry will be free too. The resulting targeting problem reads

$$r(\theta_f; \xi, \theta_A) - r_f = 0 \quad (5)$$

$$t(\theta_f; \xi, \theta_A) - t_f = 0, \quad (6)$$

and the system is solved for (ξ, θ_A) using an iterative method and given the initial conditions $(r_0, v_0, \theta_0, \psi_0)$ and the boundary conditions (r_f, t_f) . For robustness, θ_A is defined as a fraction of the angle $\theta_f - \theta_0$.

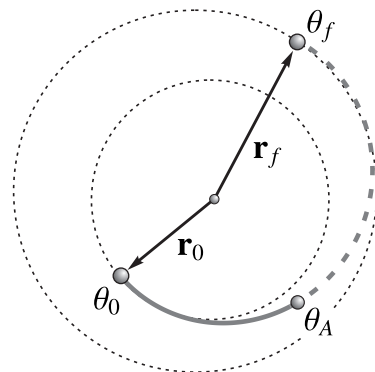


Figure 2: Geometry of a thrust-coast leg, with the dashed line showing the coast arc

Rendezvous mode

Note that in the approach described above the velocity of the spacecraft when arriving to the final body is not constrained and it can take arbitrary values. This methodology will be useful when the goal of the mission is to perform a flyby of the final body. When a rendezvous is required, the method needs to be slightly modified. The arrival velocity is forced to match that of the target body, imposing constraints on v_f and ψ_f . For the problem not to be over-constrained, two additional degrees of freedom are required. The transfer leg will be decomposed in three arcs instead of just two: a generalized logarithmic spiral from θ_0 to θ_A , a coast arc from θ_A to θ_B , and a second spiral segment from θ_B to θ_f , as shown in Fig. 3.

Thanks to the conservation laws in Eqs. (2) and (3), the control parameter along the second arc can be explicitly referred to the parameters of the previous segments after matching the magnitude of the velocities:¹⁴

$$\xi_2 = \frac{[2a - r_f(1 + av_f^2)]r_B}{2a(r_B - r_f)}, \quad (7)$$

where a is the semimajor axis of the intermediate Keplerian arc. This analytic expression eliminates one of the constraint equations, $v(\theta_f) = v_f$, and the rendezvous problem reduces to

$$r(\theta_f; \xi_1, \theta_A, \theta_B) - r_f = 0 \quad (8)$$

$$t(\theta_f; \xi_1, \theta_A, \theta_B) - t_f = 0 \quad (9)$$

$$\psi(\theta_f; \xi_1, \theta_A, \theta_B) - \psi_f = 0. \quad (10)$$

The values of ξ_1 , θ_A , and θ_B are solved numerically.

Types of Variables

The global-search problem is defined by sets of variables of different nature, related to the geometry of the problem and to each particular leg:

Internal variables: they are the boundary conditions defining each leg; the initial conditions $(r_0, v_0, \theta_0, \psi_0)$, the flight time t_f , and the arrival conditions (r_f, θ_f) . If the spacecraft is supposed to rendezvous with the final body, (v_f, ψ_f) will also stem from the geometry of the problem.

Search variables: the branch and prune algorithm explores different values of the search variables in order to optimize a certain cost function. The search variables are the sequence of bodies to be explored, b_i , the dates when the spacecraft reaches each body, t_i , the hyperbolic excess velocity provided by the launcher, $v_{\infty,0}$, and the flyby altitude, h_i . Some additional variables improve the flexibility of the method: the configuration of each leg (either thrust-coast or cost-thrust in the flyby case), the direction of the flyby (prograde or retrograde), and the total number of revolutions for each leg. The values of the internal variables are obtained from the search variables, defining the boundary conditions for each individual leg.

Unknowns: an iterative procedure is required to solve each leg. In particular, Eqs. (5–6) are solved for (ξ, θ_A) in the flyby mode, and Eqs. (8–10) are solved for $(\xi_1, \theta_A, \theta_B)$ in the rendezvous case. The value of ξ_2 is given by Eq. (7).

The chart in Fig. 4 shows how the variables are organized.

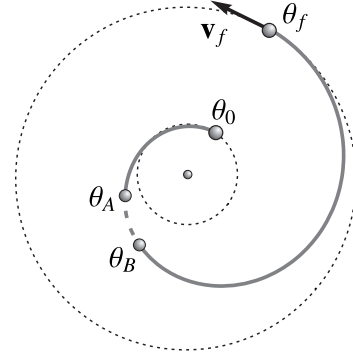


Figure 3: Rendezvous example using a thrust-coast-thrust sequence

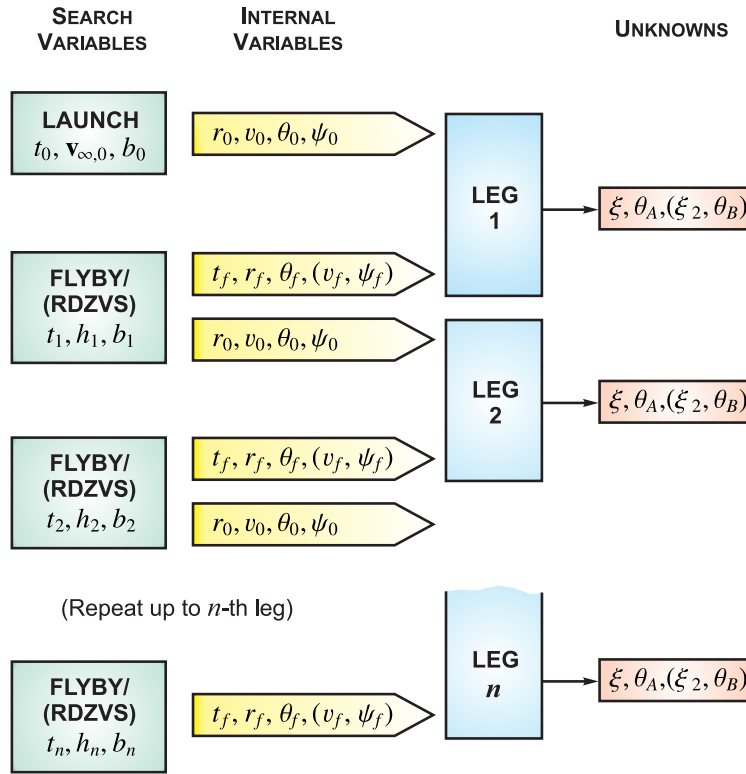


Figure 4: Schematic representation of the design strategy for a sequence of bodies b_0, b_1, \dots, b_n

Global Search: Branch and Prune

The philosophy behind the design strategy presented in this paper focuses on generating many candidate solutions, and then optimizing the promising ones. For this reason, we opted for a direct exploration of the space of solutions instead of relying on heuristic global optimization techniques. To limit the exponential growth of the dimension of the problem as the number of legs increases, solutions from the first legs are pruned before advancing to the next legs.

The first leg is defined by the departure date from body b_0 , t_0 , the launch \mathbf{v}_∞ , the time of flight, the number of revolutions, and the sequence of arcs (thrust-coast, coast-thrust, or thrust-coast-thrust). The search algorithm loops through these search variables and solves, for each combination, the corresponding leg. This stage will generate N transfer options to the second body b_1 , arriving at different dates t_1^j . The transfer options can be sorted in terms of their arrival date, so t_1^1 is the earliest arrival date and t_1^N is the latest. The interval $[t_1^1, t_1^N]$ is then divided in bins of equal size. From all the trajectories that arrive in a given bin, only the n_{sel} best solutions are selected to be further explored in the next legs. When using shape-based methods, one of the main problems is that the thrust or total Δv may not represent a realistic low-thrust profile, so the optimizer will not converge to a feasible solution. For this reason, we first discard solutions that present thrust levels over a certain threshold. Second, we prune trajectories with excessive Δv . Then, the trajectories are ranked according to the following metric,

$$J = \lambda v_{\infty,0} + \sum_{i=1}^n \Delta v_i,$$

where n is the total number of legs, λ is an arbitrary weight, and

$$\Delta v_i = \int_{t_{i-1}}^{t_i} a_p(t) dt \quad (11)$$

is the Δv due to thrust, computed by numerical quadrature.* The rest of transfer options are pruned out, reducing the number of options to be further explored in the next steps.

Figure 5 explains the algorithm graphically. The incoming trajectories from the i -th leg are grouped in their corresponding bins, represented by blue and yellow boxes. The gray trajectories are pruned out, and only the green ones are selected for further branching.

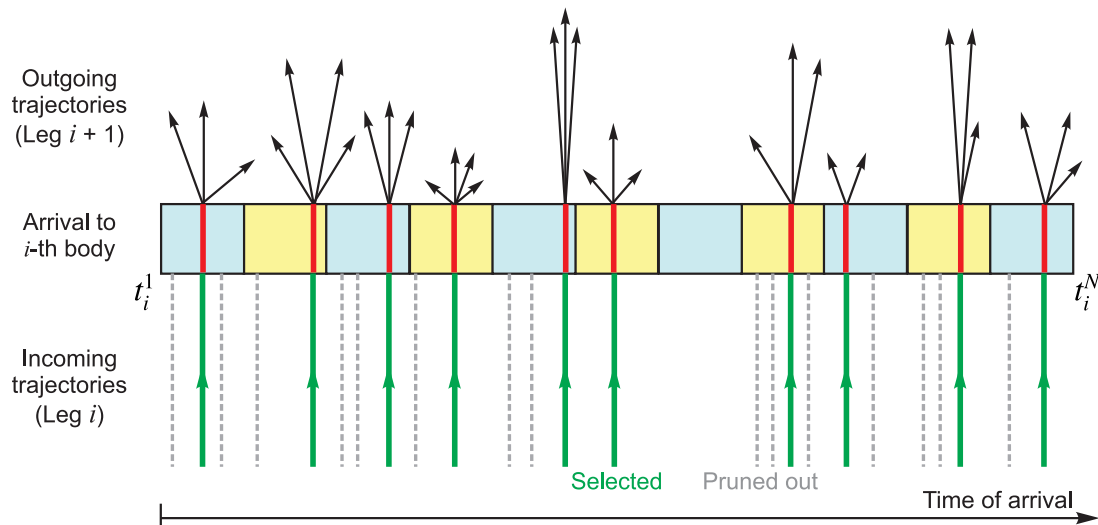


Figure 5: Branching and pruning trajectory options using arrival-date bins

Selection and Optimization

The global-search method will typically generate tens of thousands of candidate trajectories. They are then post-processed in order to rank them given a certain metric. Useful metrics are the total duration of the mission or the propellant mass fraction. In the post-processing step it is easy to compute derived quantities and sort the solutions following criteria specific to particular missions, or to impose operational constraints to discard solutions.

Initial guesses for MALTO are defined by the sequence of bodies, the dates when the bodies are reached, and the departure/arrival v -infinity vectors. The cost function that MALTO maximizes is the arrival mass. Combining the global-search tool with MALTO provides a flexible method for designing orbits, which allows the mission designer to use cost functions different from the arrival mass without the need for modifying the package for local optimization. Indeed, the metric used to select the initial guesses will bias MALTO toward solutions that are locally optimal in terms of mass, and yet close to the optimal solution in terms of the alternative cost function used to select the initial guess.

*For the case $\xi = 1/2$, Roa et al.¹⁵ provided an explicit solution to the integral in Eq. (11).

APPLICATIONS

This section presents two examples of application of the design strategy. The first example focuses on the design of an asteroid-deflection mission using a kinetic impactor. The second example seeks low-thrust gravity-assist transfer options to rendezvous with Jupiter. The main goal of these examples is to investigate how well does the semi-analytic design strategy using generalized logarithmic spirals approximate optimal low-thrust transfers, i.e. how well does the optimizer converge to a local optima given a certain initial guess.

Asteroid Deflection Mission

The fictitious hazardous asteroid (PDC2017) was generated for the risk-assessment exercise conducted during the 2017 Planetary Defense Conference. The asteroid was supposedly discovered on March 6, 2017, and its orbit is defined in Table 1. Its nominal impact date is July 21, 2027. Its orbital period of 3.4 years yields four periapsis passes between discovery and impact: May-2017, Sep-2020, Feb-2024, and Jun-2027.

Various multirevolution flyby sequences about Venus (V), Earth (E), and Mars (M) to reach the asteroid (P) have been explored using the new global-search tool. In this particular application the goal is to maximize the asteroid deflection. The deflection depends on the Δv imparted to the asteroid, which can be modeled with the figure of merit¹⁶

$$J = \beta(\mathbf{v}_{\text{ast}} \cdot \mathbf{v}_{\infty}) \frac{m_{\text{sc}}}{m_{\text{ast}}}.$$

The coefficient β adjusts the Δv accounting for ejected material from impact, and we will assume $\beta = 2$. The initial mass of the spacecraft is 6000 kg, the density of the asteroid is $\rho = 1500 \text{ kg/m}^3$ (porous rock), and its nominal radius is 100 m.

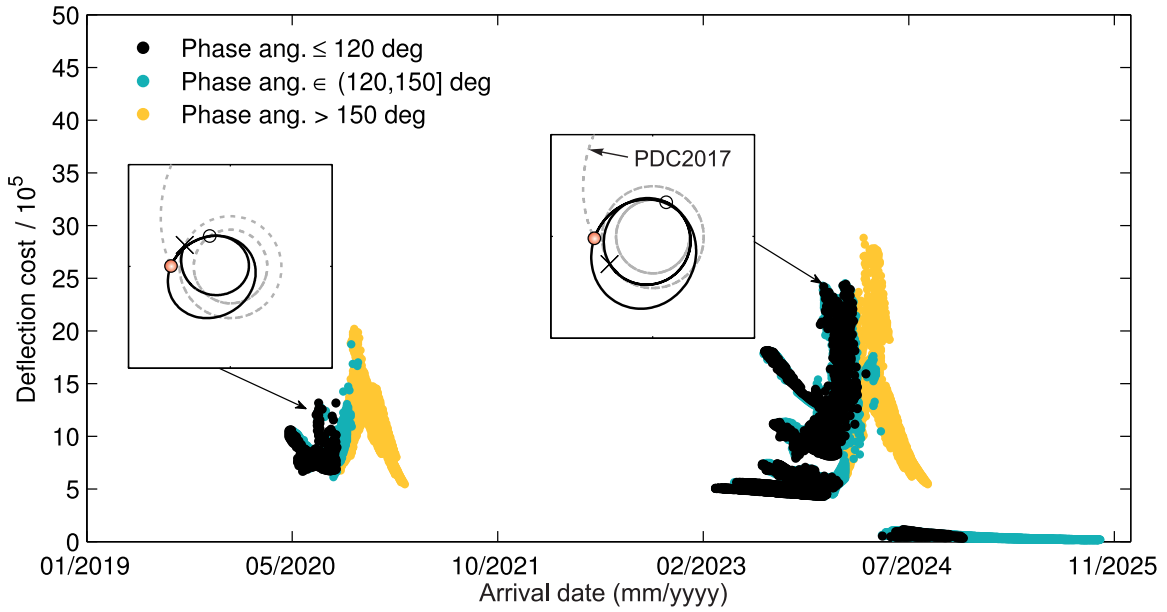
Figures 6 and 7 sort the solutions by date of arrival to the asteroid and potential deflection J . The terminal navigation phase requires the spacecraft to hit the illuminated face of the asteroid,^{9,17} which means that the Sun phase angle ϕ should be less than 120° . The solutions in the figures are classified depending on their phase angle at arrival using different colors. Initial guesses represented by black dots ($\phi < 120^\circ$) already satisfy the operational constraint. The earliest launch date that has been considered is January 1, 2019, which will leave approximately one and a half years for preparing the mission after discovery.

All four figures show that most of the converged solutions are grouped precisely around the dates of the two intermediate periapsis passages (Sep-2020 and Feb-2024). The flight time of the trajectories arriving at the first passage will be less than two years, limiting the transfer options. For this reason, most of the solutions impact the asteroid when it is around its 2024 periapsis, suggesting that this is the optimal impact region.

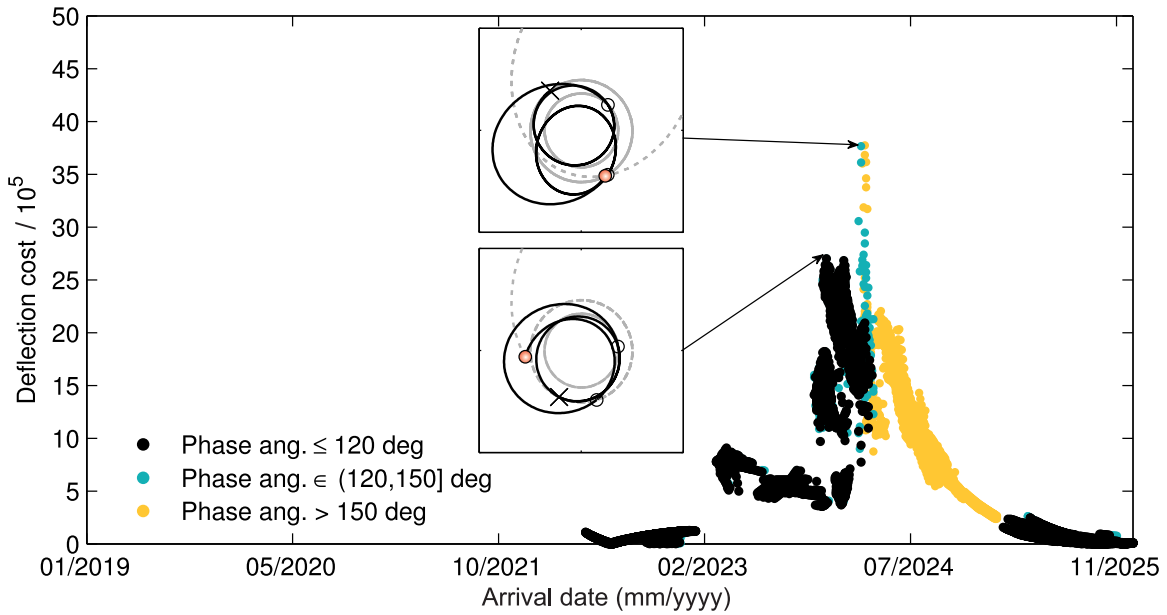
There are schematic views of example orbits overlaid on top of Figs. 6 and 7, with a red dot marking the impact point. It is worthwhile noticing that flybys are typically exploited for raising the orbit and rotating it to achieve the adequate phasing. The example of the Mars-Earth flyby sequence shows an interesting configuration in which a high launch C_3 inserts the spacecraft in an orbit beyond Mars, that is lowered by the Martian flyby and, after one complete revolution, the final

Table 1: Orbital elements of PDC2017 at the date of discovery

Element	Units	Value
a	au	2.24
e	–	0.61
i	deg	6.30
ω	deg	311.55
Ω	deg	298.13
M_0	deg	337.42

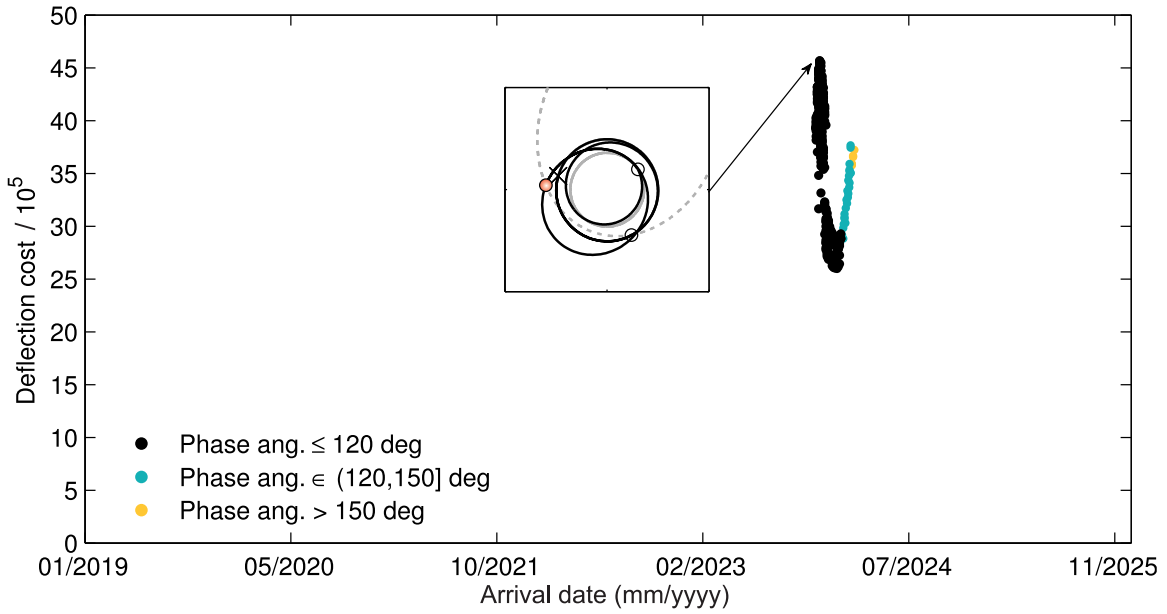


(a) Venus flyby

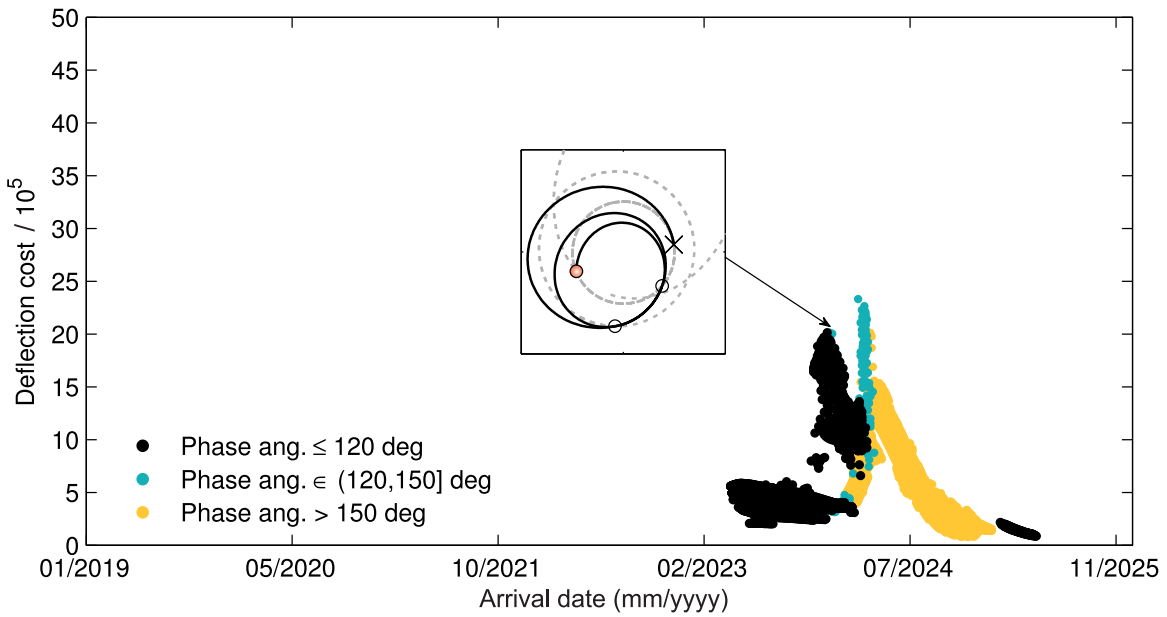


(b) Venus-Earth flyby

Figure 6: Low-thrust gravity-assist deflection options for the PDC 2017 scenario



(a) Earth-Venus flyby



(b) Mars-Earth flyby

Figure 7: Low-thrust gravity-assist deflection options for the PDC 2017 scenario (cont.)

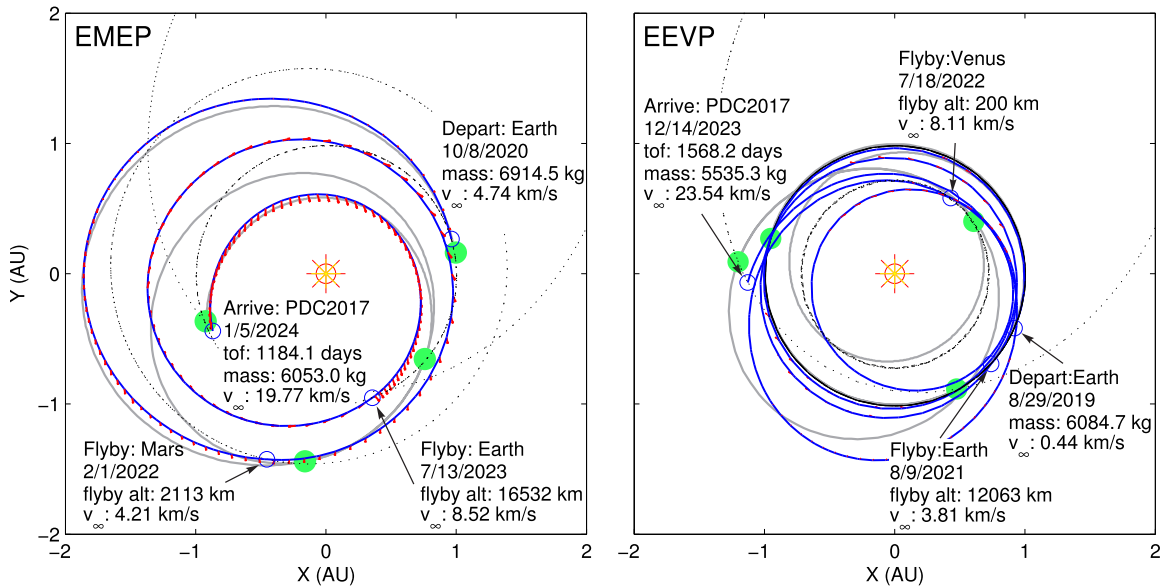


Figure 8: Optimized asteroid-deflection missions

Earth flyby lowers the apoapsis to intercept the asteroid. Also remarkable is the fact that the EEVP sequence yields less transfer options, but with a higher deflection merit J .

The most promising candidates obtained with the EMEP and EEVP sequences (highest J and $\phi < 120^\circ$) were selected for further optimization. They will be used as initial guesses for optimizing a mission using MALTO. The spacecraft is launched from the Earth using an Atlas V (551) rocket, and it is provided with two NEXT ion engines (high-thrust mode) working with $P_0 = 25$ kW. Figure 8 depicts the optimized solutions in blue, with the thrust vector represented by the red arrows and empty circles marking the position of the bodies. The gray trajectory with the bodies in green is the initial guess. The optimizer successfully found a local optima starting from the initial guess, which is qualitatively similar to the final solution.

Missions to Jupiter

This example requires the spacecraft to rendezvous with Jupiter, which imposes a constraint on the arrival velocity. When generating initial guesses, the final leg will be defined by the thrust-coast-thrust sequence, in order to satisfy the boundary conditions. Sequences of one, two, and three flybys with Venus, Earth, or Mars are considered, allowing up to two complete revolutions per leg.

The Atlas V (551) rocket is chosen as launch vehicle, and the spacecraft is provided with the same propulsion system as in the previous example (two NEXT engines), operating in high- I_{sp} mode. The objective function to maximize is the arrival mass.

Figure 10 presents the transfer maps for the single-flyby transfers, EVJ, EEJ, and EMJ, considering launch dates in a ten-year time span starting in July 2017. The maps show the propellant mass fraction required for the spacecraft to rendezvous with Jupiter, for different combinations of departure and arrival dates. In this example, two constraints are imposed on the semi-analytic solutions to reinforce their feasibility. First, a threshold of 5 N is set on the maximum thrust force. This value is above the current electric propulsion capabilities, but constraining too much the semi-analytic method could yield the loss of interesting solutions. On the other hand, without this threshold the

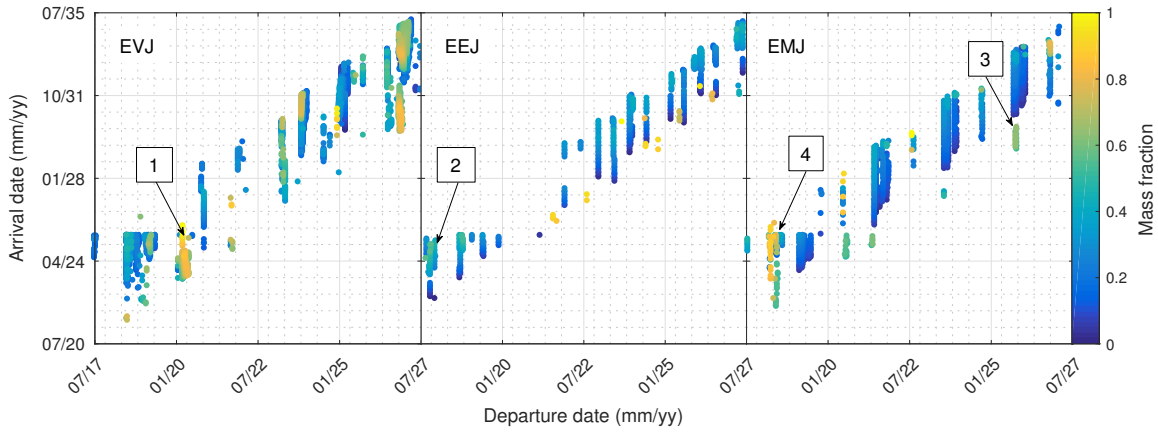


Figure 9: Mission options to rendez-vous with Jupiter (single flyby)

Table 2: Comparison of several candidate initial guesses with their optimized version

Id	Sequence	Dep. date	Arr. date	TOF (days)	C_3 (km ² /s ²)	m_0 (kg)	m_f (kg)
1_{guess}	EVJ	04/11/2020	11/21/2025	2050	9.0	–	$0.51m_0$
1_{opt}	EVJ	03/04/2019	03/30/2027	2945	34.0	3066	1446
2_{guess}	EEJ	04/02/2018	02/04/2025	2640	0.0	–	$0.33m_0$
2_{opt}	EEJ	11/11/2016	03/05/2031	5227	6.2	5449	3021
3_{guess}	EMJ	11/11/2025	05/19/2030	1650	20.3	–	$0.41m_0$
3_{opt}	EMJ	08/18/2024	08/15/2031	2552	25.0	2494	1575
4_{guess}	EMJ	08/29/2022	01/19/2030	2700	9.0	–	$0.62m_0$
4_{opt}	EMJ	03/11/2022	04/29/2030	2971	35.2	2982	1455

thrust-coast or coast-thrust sequences could degenerate into very short arcs high thrust values, closer to impulsive maneuvers than to actual low-thrust transfers. Second, the total Δv of the mission cannot exceed ten times the Δv imparted by a constant thrust of 300 mN for the same mission duration. This simplified estimate provides a reference to limit the change of the orbit’s energy. The duration of the mission is limited to 15 years.

The EVJ case reveals two promising launch windows in early 2020 and mid 2027, and the EMJ sequence suggests launch windows in early 2018 and 2021. Choosing an Earth flyby yields a number of high-efficiency solutions scattered throughout the entire time span. Four candidates are selected for further optimization, and the result is shown in Fig. 10. The blue line is the optimized trajectory, the small red arrows are the thrust vectors, and the empty circles show where the planets are. Under the optimal solution, the initial guess is plotted in gray and with green dots for the planets. MALTO successfully converged to local optima from the selected initial guesses. Case 2 has been selected as an interesting example of a more complicated multirevolution solution, in which MALTO delays the arrival date by half a revolution (~ 6 yrs), in order to converge to an optimal solution that delivers a much heavier spacecraft at the cost of exhausting the maximum mission duration allowed. Table 2 helps to compare the initial guesses with the optimal solutions. MALTO can change the launch date freely, and in these examples the dates were shifted up to 1.5 years.

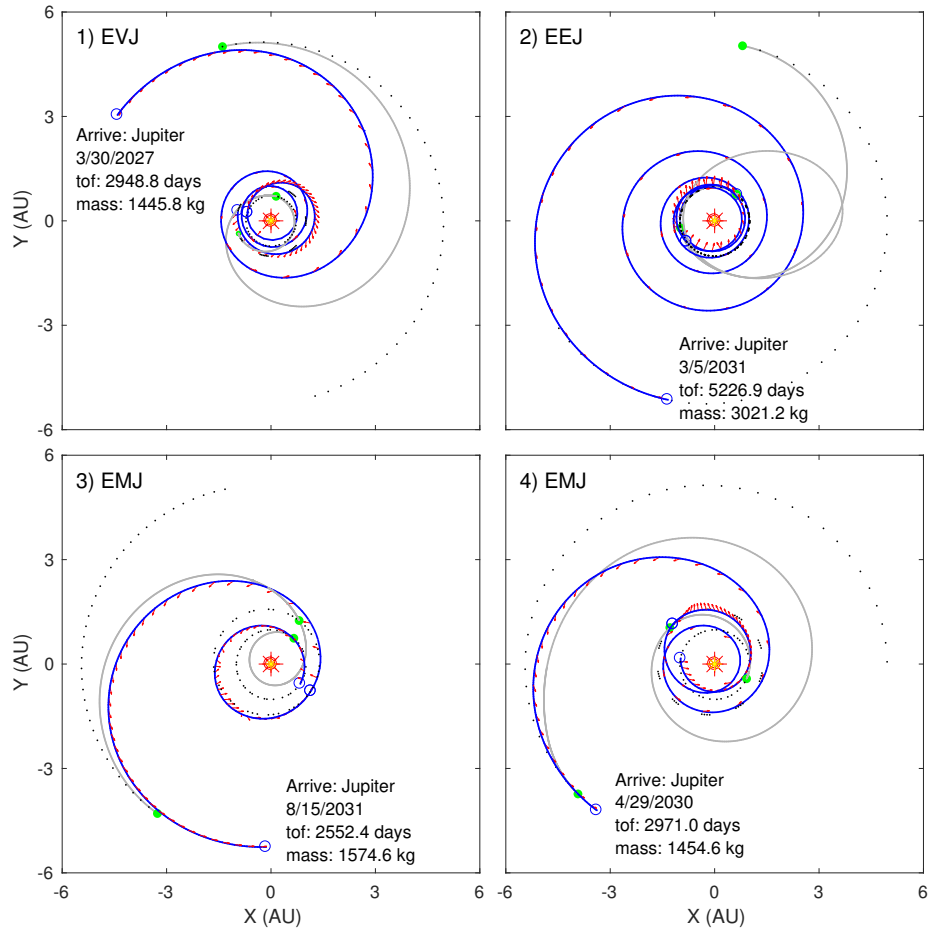


Figure 10: Candidate initial guesses and optimized solutions to rendezvous with Jupiter via one single flyby

The maps in Fig. 11 show mission options involving two gravity assist maneuvers, having extended the time-span to 20 years. The points marked with an arrow are selected for further optimization, and the resulting optimal transfers with the corresponding initial guess are depicted in Fig. 10. For the EVVJ sequence, the global search found a resonant double flyby with Venus which raises the orbit sequentially. The same strategy is adopted by MALTO when optimizing the orbit, and the optimal solution also exhibits two resonant flybys. For the EVEJ, EEVJ, and EMVJ the arrival date only changes by a few months, and remains close to the one predicted by the initial guess. In the EMEJ case, the optimizer added one extra revolution to the transfer to improve its performance.

CONCLUSIONS

Generalized logarithmic spirals combined with Keplerian arcs provide realistic representations of low-thrust transfer orbits. The initial guesses are typically close enough to a local optima for the optimizer to find a feasible solution. The method is based on the same principles as algorithms for the design of purely impulsive trajectories, which might simplify its implementation. Although the search tool computes only planar transfers, this limitation is not critical in practical interplanetary mission design problems targeting low inclination orbits. The arrival dates predicted by the initial guesses typically differ from the optimized solutions in less than a quarter of the orbital period of the target body, and the optimizer successfully converges to a local optima.

The versatility of the global search makes the technique useful for tackling mission design problems of different nature. The solutions found with the search algorithm can be post-processed as required, and ranked or discarded according to any criteria. Thanks to using analytic solutions that admit conservation laws, operational constraints can be easily imposed during the global-exploration stage. The early pruning of unfeasible branches reduces the dimension of the search problem, speeding up the process.

ACKNOWLEDGMENTS

The authors wish to thank Damon Landau for his insights on the branch and prune algorithm. This research was carried out at the Jet Propulsion Laboratory, California Institute of Technology, under a contract with the National Aeronautics and Space Administration.

APPENDIX: GENERALIZED LOGARITHMIC SPIRALS

First, transform to the new variables

$$\tau = \frac{t}{\beta}, \quad \tilde{r} = \frac{r}{\alpha}, \quad \tilde{v} = \frac{v}{\delta}, \quad \kappa_1 = \frac{K_1}{\delta^2}, \quad \kappa_2 = \frac{K_2}{\alpha\delta^2}.$$

Elliptic spirals ($\kappa_1 < 0$)

Elliptic spirals never to escape the gravitational well of the attracting body. There is a maximum radius

$$\tilde{r}_{\max} = \frac{1 - \kappa_2}{(-\kappa_1)},$$

which is called the apoapsis of the spiral. The trajectory is given by

$$\frac{\tilde{r}(\theta)}{\tilde{r}_{\max}} = \frac{1 + \kappa_2}{1 + \kappa_2 \cosh \beta(\theta)}$$

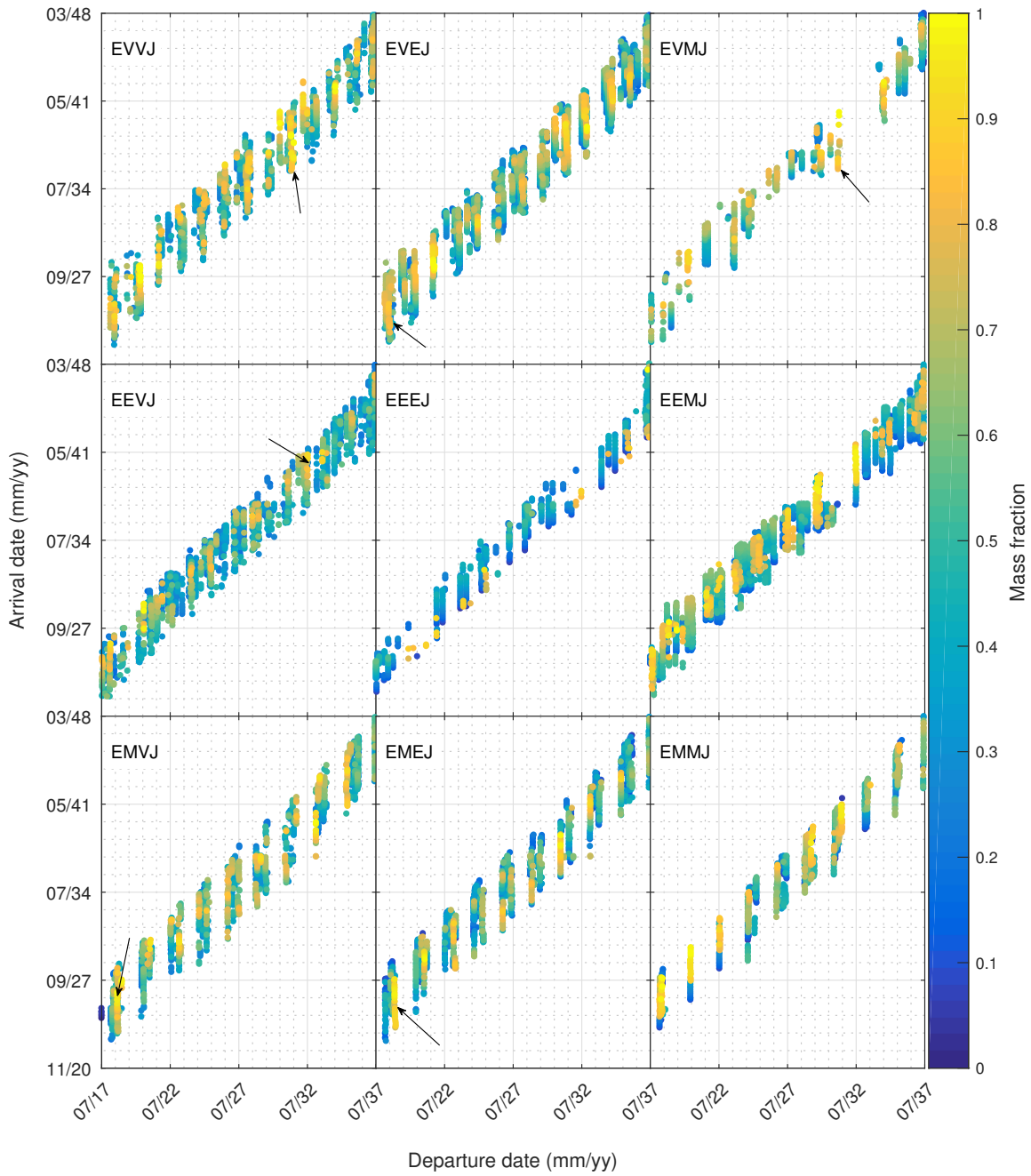


Figure 11: Mission options to Jupiter including two flybys

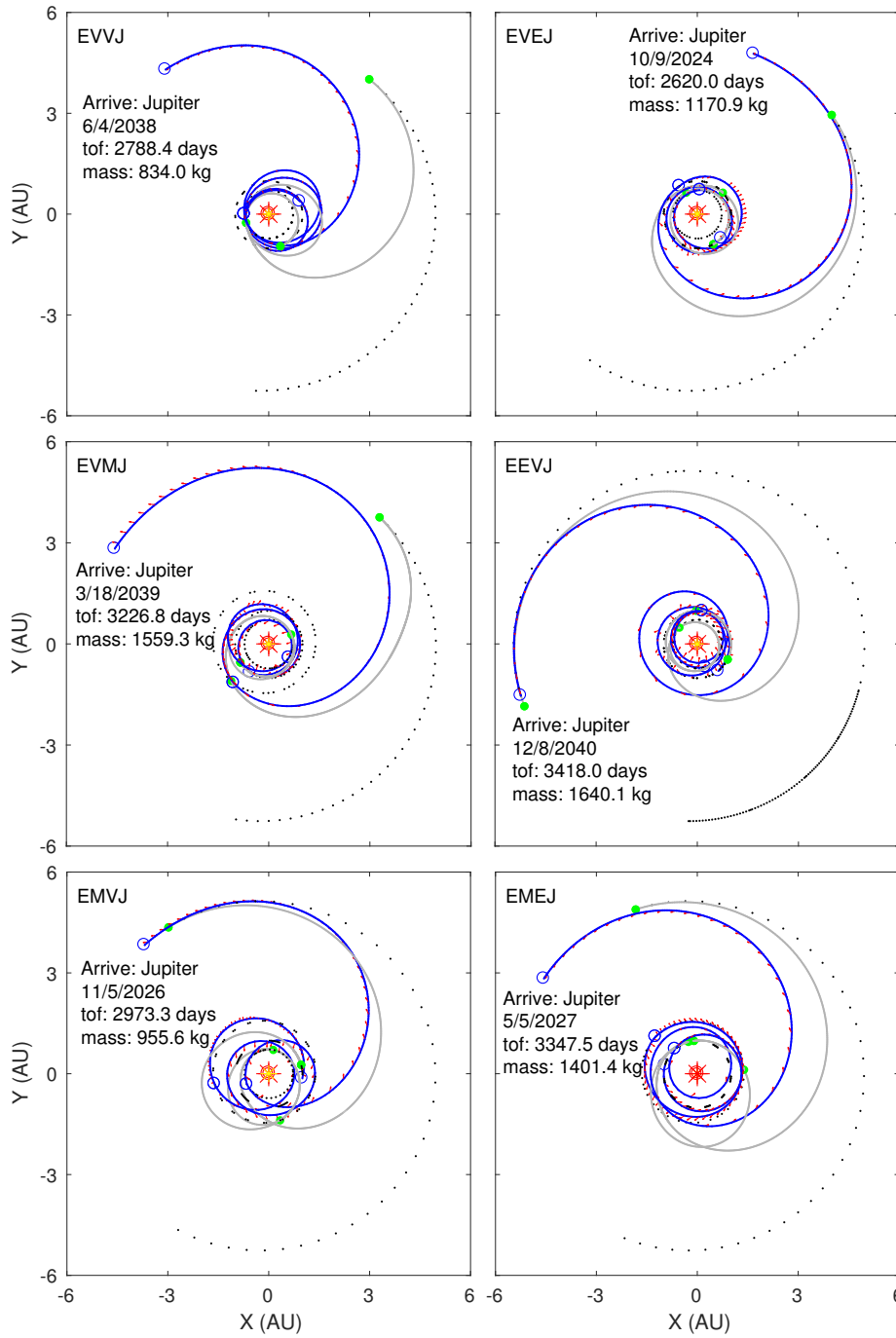


Figure 12: Candidate initial guesses and optimized solutions to rendezvous with Jupiter with two flybys

having introduced the spiral anomaly:

$$\beta(\theta) = \frac{\ell}{\kappa_2}(\theta - \theta_m), \quad \text{with } \ell = \sqrt{1 - \kappa_2^2}.$$

The angle θ_m is the orientation of the apoapsis and can be solved from the initial conditions

$$\theta_m = \theta_0 \pm \frac{\kappa_2}{\ell} \left| \operatorname{arccosh} \left\{ \frac{\tilde{r}_{\max}}{\tilde{r}_0} - \frac{1}{\kappa_2} \left(1 - \frac{\tilde{r}_{\max}}{\tilde{r}_0} \right) \right\} \right|.$$

The first sign is chosen if the spiral is initially in raising regime, and the second if it is in lowering regime.

The time of flight is written as a function of the radial distance:

$$\tau(\tilde{r}) - \tau_m = \pm \frac{\tilde{r}\tilde{v}}{\kappa_1} \sqrt{\frac{1 - \sin \psi}{1 + \sin \psi}} \pm \frac{\sqrt{2}[k'^2 \Delta \Pi - \kappa_2 \Delta E]}{(-\kappa_1)^{3/2} \sqrt{\kappa_2}}.$$

It is referred to the time of apoapsis passage, denoted τ_m . The solution is given in terms of the complete and the incomplete elliptic integrals of the second, $E(\phi, k)$, and third kinds, $\Pi(p; \phi, k)$, namely

$$\Delta E = E(\phi, k) - E(k), \quad \Delta \Pi = \Pi(p; \phi, k) - \Pi(p; k).$$

Their argument, modulus and parameter are, respectively,

$$\sin \phi = \frac{\tilde{v}_m}{\tilde{v}} \sqrt{\frac{2}{1 + \sin \psi}}, \quad k = \sqrt{\frac{-\kappa_1 \tilde{r}_{\max}}{2}}, \quad p = \frac{\kappa_1 \tilde{r}_{\max}}{2\kappa_2}.$$

The complementary modulus k' is defined as $k' = \sqrt{1 - k^2}$.

The time of apoapsis passage τ_m is computed initially from the initial conditions like

$$\tau_m = \mp \frac{\tilde{r}_0 \tilde{v}_0}{\kappa_1} \sqrt{\frac{1 - \sin \psi_0}{1 + \sin \psi_0}} \mp \frac{\sqrt{2}[k'^2 \Delta \Pi_0 - \kappa_2 \Delta E_0]}{(-\kappa_1)^{3/2} \sqrt{\kappa_2}}.$$

The first sign corresponds to raising regime, and the second to lowering regime.

Parabolic spirals ($\kappa_1 = 0$)

When κ_1 vanishes the velocity in the spiral reduces to $\tilde{v} = 1/\sqrt{\tilde{r}}$. The trajectory is simply

$$\tilde{r}(\theta) = \tilde{r}_0 e^{(\theta - \theta_0) \cot \psi}.$$

The time of flight reduces to

$$\tau(\tilde{r}) - \tau_0 = \pm \frac{2}{3\ell} (\tilde{r}^{3/2} - \tilde{r}_0^{3/2}).$$

It is referred directly to the initial conditions and requires no further computations.

Hyperbolic spirals ($\kappa_1 > 0$)

Hyperbolic spirals are defined by $\kappa_1 > 0$, which makes

$$\tilde{v}_\infty^2 = \kappa_1.$$

The constant κ_1 is equivalent to the characteristic energy C_3 .

There are two types of hyperbolic spirals: Type I spirals, $\kappa_2 < 1$, only have one asymptote, which means that a spiral in raising regime escapes and a spiral in lowering regime falls to the origin; Type II spirals, $\kappa_2 > 1$, have two asymptotes. The particle approaches the origin from an asymptote, reaches a minimum radius $\tilde{r}_{\min} \neq 0$, transitions to raising regime and then escapes along a symmetric asymptote.

Hyperbolic spirals of Type I

Since there are no axes of symmetry in this family of solutions the spiral anomaly is redefined with respect to the orientation of the asymptote as

$$\beta(\theta) = \pm \frac{\ell}{\kappa_2} (\theta_{\text{as}} - \theta).$$

Here, θ_{as} provides the asymptote. It is defined from the initial conditions

$$\theta_{\text{as}} = \theta_0 \pm \frac{\kappa_2}{\ell} \ln \left[\frac{\kappa_2(\zeta - \ell - \kappa_2 \sin \psi_0 + \ell |\cos \psi_0|)}{\tilde{r}_0 \kappa_1 \zeta \sin \psi_0} \right] \quad (12)$$

in terms of the parameter $\zeta = 1 + \ell$.

The equation of the trajectory is

$$\tilde{r}(\theta) = \frac{\zeta \ell^2 / \kappa_1}{\sinh \frac{\beta}{2} \left[2\zeta \sinh \frac{\beta}{2} + (\zeta^2 - \kappa_2^2) \cosh \frac{\beta}{2} \right]}.$$

The time of flight for the case $\kappa_1 > 0$ and $\kappa_2 < 1$ becomes

$$\tau(\tilde{r}) = \kappa_4 \pm \left\{ \frac{\tilde{r}\tilde{v}}{\kappa_1} \sqrt{\frac{1 + \sin \psi}{1 - \sin \psi}} - \frac{\sqrt{2} \{E - (1 - p)\Pi\} \sqrt{\kappa_2}}{\kappa_1^{3/2}} \right\}$$

written in terms of a constant κ_4 , which is easily solved by particularizing the previous equation at $\tau = 0$. The solution is given in terms of the incomplete elliptic integrals of the second and third kinds, $E = E(\phi, k)$ and $\Pi = \Pi(p; \phi, k)$, with:

$$\sin \phi = \sqrt{\frac{\kappa_1 \tilde{r} \sin \psi}{p \kappa_2 (1 - \sin \psi)}}, \quad k = \frac{1}{2} \sqrt{2(1 + \kappa_2)}, \quad p = \frac{1 + \kappa_2}{2\kappa_2}.$$

Hyperbolic spirals of Type II

The periapsis radius takes the form

$$\tilde{r}_{\min} = \frac{\kappa_2 - 1}{\kappa_1}.$$

The periapsis of the spiral defines an axis of symmetry, oriented as θ_m :

$$\theta_m = \theta_0 \mp \frac{\kappa_2}{\ell} \left\{ \frac{\pi}{2} + \arctan \left[\frac{1 - \kappa_2 \sin \psi_0}{\ell |\cos \psi_0|} \right] \right\}.$$

As always, the first sign corresponds to raising regime and the second to lowering regime. With this angle the spiral anomaly is defined as

$$\beta(\theta) = \frac{\ell}{\kappa_2} (\theta - \theta_m).$$

The parameter ℓ is redefined as $\ell = \sqrt{\kappa_2^2 - 1}$ for the signs to be compatible.

The equation of the trajectory is

$$\frac{\tilde{r}(\theta)}{\tilde{r}_{\min}} = \frac{1 + \kappa_2}{1 + \kappa_2 \cos \beta(\theta)}$$

Due to the denominator in this expression two asymptotes appear naturally,

$$\theta_{\text{as}} = \theta_m \pm \frac{\kappa_2}{\ell} \left\{ \frac{\pi}{2} + \arctan \frac{1}{\ell} \right\}.$$

The particle escapes to infinity along the asymptote defined by the (+) sign, and comes from infinity along the asymptote defined by the (-) sign.

Finally, the time of flight reads

$$\begin{aligned} \tau(\tilde{r}) - \tau_m = \mp & \left\{ \frac{(\kappa_2 + 1)\kappa_2 E - \kappa_1 \tilde{r}_{\min} [\kappa_2 F + \Pi]}{\kappa_1 \sqrt{\kappa_1 \kappa_2 (\kappa_2 + 1)}} \right. \\ & \left. + \frac{1}{\kappa_1^{3/2}} \operatorname{arcsinh} \left[\frac{\sqrt{\kappa_1 \tilde{r} (\tilde{r}^2 - \kappa_2)}}{\sqrt{2\kappa_2 \tilde{r}^2 + (\tilde{r}^2 - \kappa_2)}} \right] - \frac{\tilde{v}}{\kappa_1^2} \sqrt{\tilde{r}^2 \tilde{v}^4 - \kappa_2^2} \right\}. \end{aligned} \quad (13)$$

It is given in terms of the incomplete elliptic integrals of the first, $F \equiv F(\phi, k)$, second, $E \equiv E(\phi, k)$, and third kinds, $\Pi \equiv \Pi(p; \phi, k)$. The argument of the elliptic integrals in this case is

$$\sin \phi = \frac{\sqrt{(1 - \sin \psi)}}{k \sqrt{\kappa_2 - \sin \psi}}, \quad k = \sqrt{\frac{2}{\kappa_2 + 1}}, \quad p = \frac{1}{\kappa_2}.$$

The time of periapsis passage τ_m can be easily solved from Eq. (13) particularized at $\tau = 0$.

Transition between Type I and Type II hyperbolic spirals

Hyperbolic spirals of Type I have been defined for $\kappa_2 < 1$, whereas $\kappa_2 > 1$ yields hyperbolic spirals of Type II. In the limit case $\kappa_2 = 1$ the equations of motion simplify noticeably; the resulting spiral is

$$\tilde{r}(\theta) = \frac{2}{\kappa_1 \beta (\beta \mp 2)}$$

In this case the angular variable $\beta(\theta)$ is defined with respect to the orientation of the asymptote. That is

$$\beta = \theta - \theta_{\text{as}}.$$

The asymptote is fixed by

$$\theta_{\text{as}} = \theta_0 \mp \left(1 - \sqrt{1 + \frac{2}{\kappa_1 \tilde{r}_0}} \right).$$

The time of flight is no longer given by elliptic integrals. It reduces to

$$\tau(\tilde{r}) - \tau_0 = \pm \frac{1}{\kappa_1^{3/2}} \left\{ \Xi - \Xi_0 + \frac{1}{2} \ln \left[\frac{2(\tilde{r}_0 \tilde{v}_0^2 + \Xi_0) + 1}{2(\tilde{r} \tilde{v}^2 + \Xi) + 1} \right] \right\}.$$

The auxiliary parameter $\Xi = \Xi(\tilde{r})$ reads $\Xi(\tilde{r}) = \tilde{v} \sqrt{\tilde{r}(\tilde{r} \tilde{v}^2 + 1)}$. The equation for the time of flight has been referred directly to the initial conditions for convenience.

REFERENCES

- [1] Massimiliano Vasile. A global approach to optimal space trajectory design. *Advances in the Astronautical Sciences*, 114:629–647, 2003.
- [2] Dario Izzo, Victor M Becerra, Darren R Myatt, Slawomir J Nasuto, and J Mark Bishop. Search space pruning and global optimisation of multiple gravity assist spacecraft trajectories. *Journal of Global Optimization*, 38(2):283–296, 2007.
- [3] Anastassios E Petropoulos, James M Longuski, and Nguyen X Vinh. Shape-based analytic representations of low-thrust trajectories for gravity-assist applications. In *AAS/AIAA Astrodynamics Specialist Conference*, pages 563–581, 1999.
- [4] Dario Izzo. Lambert’s problem for exponential sinusoids. *Journal of Guidance, Control, and Dynamics*, 29(5):1242–1245, 2006.
- [5] Anastassios E Petropoulos and Jon A Sims. A review of some exact solutions to the planar equations of motion of a thrusting spacecraft. In *2nd International Symposium Low Thrust Trajectories, Toulouse, France, June 2002*.
- [6] M Vasile, O Schütze, O Junge, G Radice, M Dellnitz, and D Izzo. Spiral trajectories in global optimisation of interplanetary and orbital transfers. *Ariadna Study Report AO4919*, 5:4106, 2006.
- [7] P De Pascale and M Vasile. Preliminary design of low-thrust multiple gravity-assist trajectories. *Journal of Spacecraft and Rockets*, 43(5):1065–1076, 2006.
- [8] DJ Gondelach and R Noomen. Hodographic-shaping method for low-thrust interplanetary trajectory design. *Journal of Spacecraft and Rockets*, 52(3):728–738, 2015.
- [9] Anastassios E Petropoulos. Low-thrust orbit transfers using candidate Lyapunov functions with a mechanism for coasting. In *AIAA/AAS Astrodynamics Specialist Conference and Exhibit*, number 04-5089, 2004.
- [10] Javier Roa, Jesús Peláez, and Juan Senent. New analytic solution with continuous thrust: generalized logarithmic spirals. *Journal of Guidance, Control, and Dynamics*, 39(10):2336–2351, 2016.
- [11] Javier Roa. Nonconservative extension of Keplerian integrals and a new class of integrable system. *Monthly Notices of the Royal Astronomical Society*, 463(3):3204–3219, 2016.
- [12] Jon A Sims and Steve N Flanagan. Preliminary design of low-thrust interplanetary missions. In *AAS/AIAA Astrodynamics Specialist Conference, AAS Paper*, pages 99–338, 1999.
- [13] Jon A Sims, Paul A Finlayson, Edward A Rinderle, Matthew A Vavrina, and Theresa D Kowalkowski. *Implementation of a low-thrust trajectory optimization algorithm for preliminary design*. Pasadena, CA: Jet Propulsion Laboratory, National Aeronautics and Space Administration, 2006.
- [14] Javier Roa. *Regularization in Astrodynamics: applications to relative motion, low-thrust missions, and orbit propagation*. PhD thesis, Technical University of Madrid, September 2016, Chapter 11.
- [15] Javier Roa, Jesús Peláez, and Juan Senent. Spiral Lambert’s problem. *Journal of Guidance, Control, and Dynamics*, 39(10):2250–2263, 2016.
- [16] Daniel Grebow, Damon Landau, Shyam Bhaskaran, Paul Chodas, Steven Chesley, Don Yeomans, Anastassios Petropoulos, Jon Sims, et al. Deflection missions for asteroid 2011 ag5. 2012.
- [17] Shyam Bhaskaran, Steven Chesley, Sang Park, Anastassios Petropoulos, Jon Sims, Donald Yeomans, and Robert Haw. Navigation challenges of a kinetic energy asteroid deflection spacecraft. In *AIAA/AAS Astrodynamics Specialist Conference and Exhibit*, page 6254, 2008.